On the use of the eXtended Finite Element Method with Quatree/Octree meshes

Grégory Legrain, Raphaël Allais, Patrice Cartraud

GeM Institute

GeM Institute UMR CNRS 6183
École Centrale de Nantes / Université de Nantes / CNRS,
1 Rue de la Noë, BP92101, 44321 Nantes, France.

On the use of the eXtended Finite Element Method with Quatree/Octree meshes

G. Legrain, R. Allais and P. Cartraud

Preprint submitted to:
International Journal for Numerical Methods in Engineering

On the use of the eXtended Finite Element Method with Quatree/Octree meshes

G. Legrain[1], R. Allais and P. Cartraud

GeM Institute UMR CNRS 6183 - École Centrale de Nantes / Université de Nantes / CNRS, 1 Rue de la Noë, BP92101, 44321 Nantes, France.

SUMMARY

This paper describes the use of the eXtended Finite Element Method in the context of quadtree/octree meshes. Particular attention is paid on the enrichment of hanging nodes that inevitably arise with these meshes. An approach for enforcing displacement continuity along hanging edges and faces is proposed and validated on various numerical examples (holes, material interfaces and singularities) in both 2D and 3D.

Preprint submitted to: International Journal for Numerical Methods in Engineering

KEY WORDS: eXtended Finite Element Method, Partition of Unity, Hanging nodes, Octree, Quadtree, Nitsche approach

1. INTRODUCTION

Recently, much attention has been paid on adaptivity in the context of partition of unity finite element methods [1]. Adaptivity allows to improve the accuracy of the numerical solution at a lower computational cost. The objective is to obtain an efficient nodes distribution (both for their number and location). Once the error distribution is known, the mesh is refined, and the process is re-itered until the error falls below a threshold value on the whole mesh. Various approaches have been developed for mesh adaptation [2]: The adaptation may be global with the creation of an element-size specification defined on a background mesh that is used to rebuild the whole (unstructured) mesh, or it can be local if only the elements above the error threshold are locally subdivided. In this contribution, we rely on a quadtree/octree data structure which is a simple, fast and efficient approach for h-refinement. Quatree/octree data structures are based on

[1]Correspondence to: Grégory Legrain, GeM Institute, 1 Rue de la Noë, BP92101, 44321 Nantes, France. gregory.legrain@ec-nantes.fr

0

Contract/grant sponsor: Publishing Arts Research Council; contract/grant number: 98–1846389

a recursive decomposition of the elements that exceed the prescribed error tolerance. However, this approach leads to so called "hanging nodes" if an element and its neighbors have not the same size. Various approaches have been proposed in classical finite elements in order to enforce the compatibility of the approximation [3, 4, 5, 6]. Here, we consider the case of the eXtended Finite Element Method [7]. This method is part of Partition of Unity finite element methods [1, 7, 8], that generalize classical finite elements by enabling to incorporate *a priori* informations on the nature of the solution. The X-FEM was developed to overcome the necessity of geometrical conformity when using the finite element method. Its first application was in the context of problems exhibiting strong discontinuities such as fracture mechanics [7, 9]. From 2D linear elastic fracture mechanics, the method was further extended to 3D [10, 11, 12] and non-linear fracture mechanics [13, 14, 15, 16, 17]. The method was also developed to handle holes [18], material interfaces [18, 19, 20] and flows [21, 22] independently of the finite element mesh. Lately, problems involving stability conditions [15, 23, 24, 25] and error estimation [26, 27, 28, 29, 30, 31] have been considered. Among partition of unity finite element methods, one can cite also the Generalized Finite Element Method (GFEM) [32, 8] that has been used for a wide class of applications. In particular, the use handbook functions makes possible to enrich the approximation in the case where the enrichment functions are not explicitly known [33, 34]. Even if the use of the X-FEM improves the accuracy of the approximation in critical area, this does not eliminate the need for controlling the error which implies remeshing.

Here, we investigate the coupling of the X-FEM and a quadtree/octree data structure for adaptive computation driven by the local error. The main issue still comes from the appearance of hanging nodes in the approximation, and the way the corresponding degrees of freedom have to be treated. In this context, Tabarraei and Sukumar [6, 35] have proposed to consider the elements containing hanging nodes as counterpart of a polygonal reference element through an iso-parametric mapping. This approach proved to be effective for the examples the authors provided. One drawback is related to the integration of the stiffness matrix over arbitrary polygons: the authors proposed to split the reference space in several simplices, and perform the integration on these sub-elements. Recently, Natarajan et al. [36] proposed an alternative based on Schwarz-Christoffel mapping which eliminated the need for two the successive mappings. However, the extension of this special mapping to 3D has not been discussed. Another strategy was proposed by Alizada and Fries [37] which consists in creating special elements that allows to associate explicitly degrees of freedom to the hanging nodes. This approach is appealing in 2D, but seems difficult to extend in 3D because of all the special cases that can occur, depending on the number of hanging nodes (in 3D, nodes can hang both on faces or on edges). In this paper, a strategy based on the use of classical finite elements is proposed. The continuity of the finite element field is ensured even on interfaces containing hanging nodes. The idea consists in selecting the right degrees of freedom for the enrichment, then properly constrain them to ensure the continuity of the finite element field. The choice of the dofs to be enriched is obtained by virtually introducing composite elements, that are practically treated using linear combination of classical shape functions. Note that the spirit of the approach proposed here shares similarities with

the work of Sukumar and Park [38] that deals with the enforcement of Bloch-periodic boundary conditions.

The paper is organized as follows: In a first part, basic ingredients of quadtree/octree data structure are presented with a particular focus on the approaches that can be used to enforce the conformity of the field across interfaces containing hanging nodes. Then the X-FEM is presented, and the case of holes, material interfaces and cracks is considered. In a third part, an approach that ensures continuity of the enriched field across hanging elements is presented, and validated on various numerical examples in both 2D and 3D.

2. OCTREE / QUATREE DATA STRUCTURE

Quadtree (resp. Octree) is a spatial decomposition method that consists in subdividing recursively the 2D (resp. 3D) bounding-box of the domain of interest (Ω) [2]. This box is first subdivided into four equally-sized cells, each of which may be recursively subdivided several times (until a stopping criterion is met). The subdivision of an element is called its children whereas the subdivided element is called father. A cell that is not subdivided is called a leaf, otherwise it is called internal cell. The level of an element corresponds to the number of subdivisions required to obtain this cell from the bounding box. Note that the level of the root cell is zero (no subdivision was needed to obtain it). Two cells are called neighbor or adjacent if they share a common edge. If two adjacent cells do not share the same level, then so-called hanging nodes appear. In order to manage mesh gradation, the level difference between adjacent cells may not exceed one. This is also called the 2:1 rule (any element have at most two neighbors along its edges).

One key aspect of quadtree/octree structures is that all the topological informations can be stored as a tree. Using this structure, informations such as level, neighbors, ancestors and children of an element can be easily obtained. Note that the implementation used in this paper is based on a linear encoding of the tree [2].

Quadtree/Octree were intensively used in the context of computer graphics or image processing. They were first used in the context of finite elements by Yerry and Sheppard [39]. An appealing feature in this context stems from the fact that all the elements are geometrically homothetic: in 2D, the elementary stiffness matrix is the same for all the elements and a unique computation is sufficient for the assembly of the whole global stiffness matrix.

However, the finite element approximation is incompatible along the edges containing hanging nodes. Classically, hanging nodes are constrained to corner nodes [3], as on these edges the coarsest element dictates the form of the approximation. Alternatively, the mesh can be modified locally to enforce the compatibility (see for example figure 2). In 2D, only five cases can occur, which makes possible mesh modification. However, mesh modifications can be computationally expensive (finding elements containing hanging nodes, inserting new elements), and the number of possible case increases a lot in 3D. To overcome this issue, Schroeder et al. [40] proposed to generate on-the-fly transitional elements near hanging nodes by mean of a local Delaunay triangulation. Krysl et al. [4] proposed a hierarchical enrichment of the basis to obtain conformity

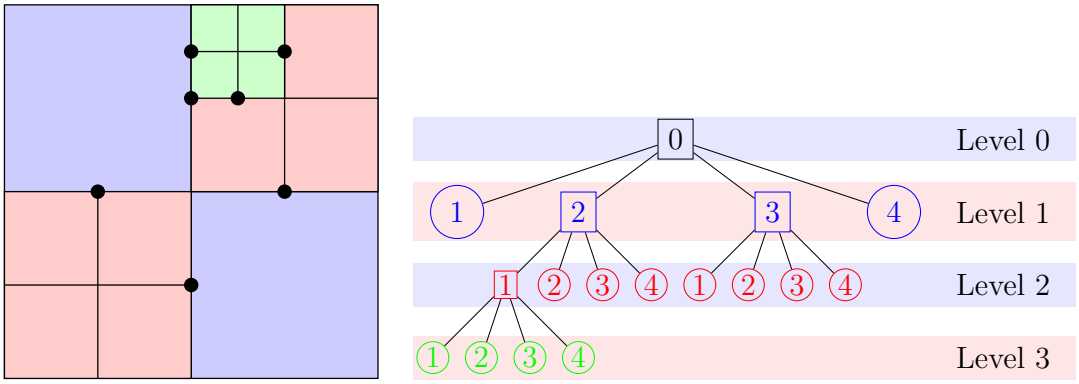

(a) (b)

Figure 1: A quadtree mesh (a) and its representative tree (b). Hanging nodes are highlighted by •. Note that in this case, the 2:1 rule is not verified.

along interfaces containing hanging nodes. The third class of approaches consists in weakly imposing the conformity by mean of penalty, Lagrange multipliers or Nitsche. Recently, new approaches have been proposed to obtain conforming approximations using quadtree meshes [5]. In particular Tabarraei and Sukumar [6] proposed the use of polygonal interpolants to produce conforming approximations with hanging nodes.

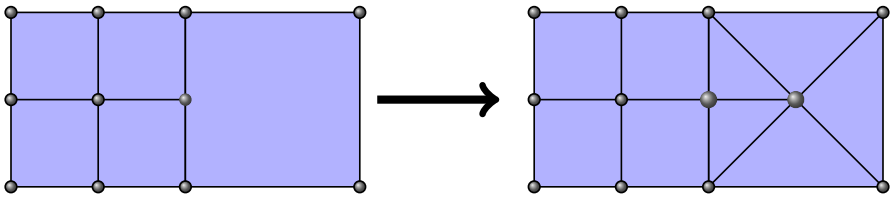

Figure 2: Mesh modification.

In this contribution, an approach based constraining the degrees of freedom of the hanging nodes is proposed in the context of the eXtended Finite Element Method. For non enriched finite elements, it reduces to a classical constraining approach, and remains usable for enriched finite elements despite of the difficulties that arise (see section 4).

3. GOVERNING EQUATIONS

In the following, 2D linear isotropic thermal problems are considered. Let $\partial\Omega$ be the boundary of the domain Ω (see figure 3). Let Γ_D and Γ_N form a disjointed partition of

$\partial\Omega$. The scalar field T, solution of the problem, verifies the following equations :

$$\lambda \cdot \Delta T + r = 0 \qquad in\ \Omega \tag{1}$$

$$T = T_D \qquad on\ \Gamma_D \tag{2}$$

$$\lambda \cdot \nabla T \cdot n = g \qquad on\ \Gamma_N \tag{3}$$

where λ is the material conductivity, r is a volumic heat source, g is a prescribed flux (Neumann boundary condition) and T_D is the prescribed temperature on Γ_D (Dirichlet boundary condition).

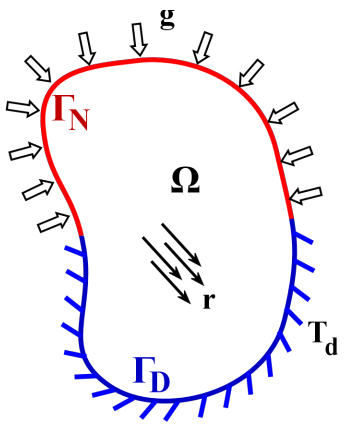

Figure 3: Domain and boundary conditions

T is searched in a standard Sobolev space $\mathcal{T} = \{T \in \mathcal{H}^1(\Omega)\,|\,T = T_D \text{ on } \Gamma_D\}$. For numerical resolution, the problem is transformed into a weak form as: find $T \in \mathcal{T}$ so that:

$$a(T, T^*) = l(T^*) \qquad \forall T^* \in \mathcal{T}^0 \tag{4}$$

where $\mathcal{T}^0$ is similar to $\mathcal{T}$ with zero Dirichlet boundary conditions, $a(\cdot,\cdot)$ and $l(\cdot)$ are respectively bilinear and linear forms defined as :

$$a(T, T^*) = \lambda \int_\Omega \nabla T \cdot \nabla T^*\ d\Omega \tag{5}$$

$$l(T^*) = \int_{\Gamma_N} g\ T^*\ d\Gamma - \int_\Omega r\ T^*\ d\Omega \tag{6}$$

4. THE EXTENDED FINITE ELEMENT METHOD

As the previous problem is generally unsolvable analytically, the solution T is sought in a finite dimensional space. Following the partition of unity framework [1], the classical

finite element space is enlarged by mean of enrichment functions. The temperature field T is searched in an approximation space $\mathcal{T}_{XFEM}$ defined by :

$$T(x) = \sum_{\alpha=1}^{n} N^{\alpha}(x) \left(T^{\alpha} + \sum_{\beta=1}^{n_e} a_{\beta}^{\alpha} \cdot \phi_{\beta} \right) \tag{7}$$

where $\langle N^{\alpha} \rangle$ and T^{α} are respectively the set of shape functions and degrees of freedom of the classical finite element approximation, $\langle \phi_{\beta} \rangle$ are enrichment functions and a_{β}^{α} the enriched d.o.f. associated to the node α and the enrichment function ϕ_{β}.

Thanks to the enrichment functions, specific behavior (such as boundary effects, voids, cracks, material interfaces for example) can be treated with a non-conforming mesh. The enrichments are chosen according to the physical phenomenon they have to represent. In this paper, three cases will be considered : cracks, holes and material interfaces.

In the case of cracks, two enrichments are used [7]: (i) A discontinuous enrichment based on a heaviside function to model crack opening across finite elements completely cut by the crack, and (ii) a singular enrichment to take into account the influence of the crack tip for node whose support contains the tip. The case of holes was addressed in [41] and [18]. It consists in an integration of the weak form only in the material part of the domain. Concerning material interfaces, the enrichment must account for the gradient jump across the interface. In [18], a distance function was used but it was shown that the convergence rate was degraded with respect to conforming finite elements, unless the approach proposed by [20] is used. Here, the so called ridge function is used (see fig.4). This function was introduced in [19] and allows to recover numerically the same convergence rate as classical finite elements.

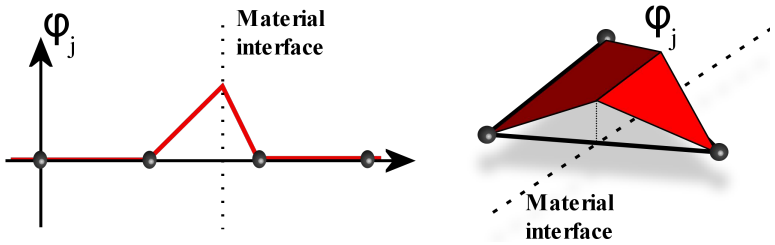

Figure 4: Ridge function for 1D and 2D problems

As presented in equation (7), the use of the X-FEM introduces enriched degrees of freedom in the approximation. In the context of octree meshes, enriched dofs could be associated to hanging nodes. For the classical dof associated to hanging nodes, strategies such as those presented in section 2 can be applied directly. However, the way enriched hanging nodes have to be taken into account is an open issue that is considered in the following section.

5. FIELD CONTINUITY ALONG HANGING EDGES / FACES

As stated in the previous section, it is not clear how do hanging nodes have to be managed in the case of X-FEM (especially their enrichment). In this section, a strategy is proposed in order to ensure the continuity of the enriched field even in the case of hanging nodes.

5.1. The case of classical finite elements

First, the case of classical finite elements is presented: Consider a cell whose neighbor's level is higher, as depicted in figure 5. Node H is hanging along the edge defined by parent nodes P_1 and P_2. Classically, the degrees of freedom associated to the hanging node H are tied to parent nodes P_1 and P_2 by mean of the following well known condition which holds for linear finite elements:

$$T^H = \frac{1}{2}\left(T^{P_1} + T^{P_2}\right) \tag{8}$$

By mean of this constraint, the continuity of the finite element field is ensured across edge P_1P_2. In fact, this condition can be viewed either as a constraint on the degrees

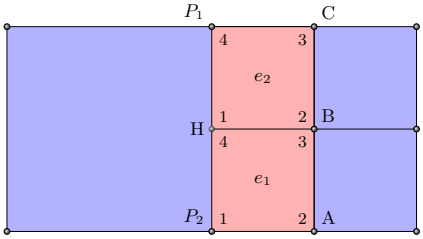

Figure 5: FEM hanging node. A, B, C, P_1, P_2: Global numbering. 1, 2, 3, 4: Local numbering.

of freedom, either as the construction of new shape functions for parent nodes P_1 and P_2 if the dof associated to the hanging node is eliminated (which amounts to merge elements e_1 and e_2). Indeed, the interpolation of the field in the two elements (e_1 and e_2) containing the hanging node can be written as:

$$\mathbf{T}(\mathbf{x})|_{\Omega_{e_1}\cup\Omega_{e_2}} = \sum_{\alpha=1}^{n} \mathbf{N}^\alpha \, T^\alpha \tag{9}$$

Where n stands for the number of nodes involved in elements e_1 and e_2. The relation above involves the dofs associated to nodes P_1, P_2, H, A, B, and C (see figure 5 for the label of the nodes). The interpolation can be written as:

$$\mathbf{T}(\mathbf{x})|_{\Omega_{e_1}\cup\Omega_{e_2}} = \mathbf{N}^{\mathbf{1}}_{\mathbf{e_1}} T^{P2} + \mathbf{N}^{\mathbf{2}}_{\mathbf{e_1}} T^{A} + \mathbf{N}^{\mathbf{3}}_{\mathbf{e_1}} T^{B} + \mathbf{N}^{\mathbf{4}}_{\mathbf{e_1}} T^{H} + \mathbf{N}^{\mathbf{1}}_{\mathbf{e_2}} T^{H} + \mathbf{N}^{\mathbf{2}}_{\mathbf{e_2}} T^{B} + \mathbf{N}^{\mathbf{3}}_{\mathbf{e_2}} T^{C} + \mathbf{N}^{\mathbf{4}}_{\mathbf{e_2}} T^{P1} \tag{10}$$

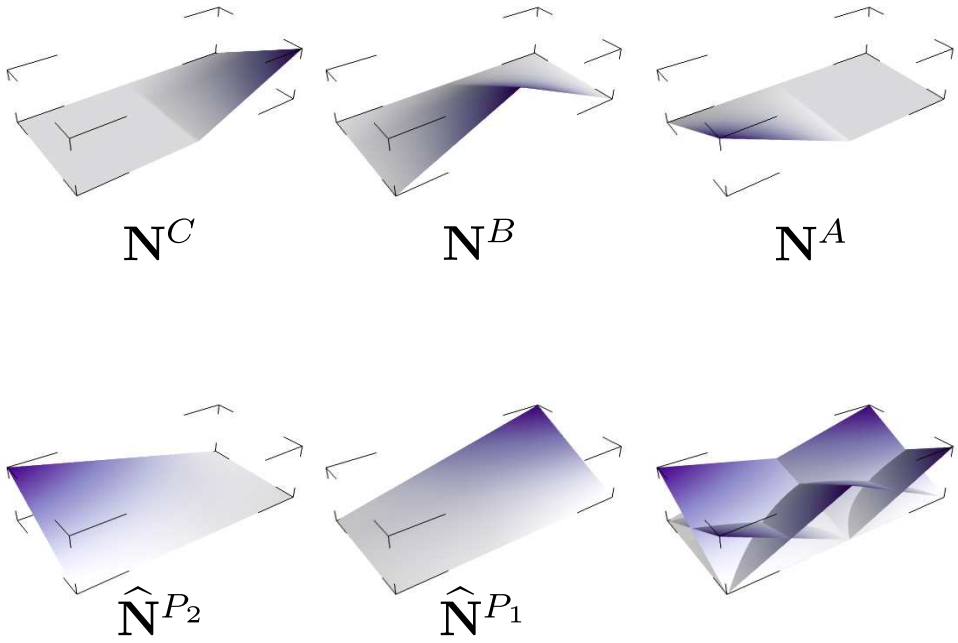

Figure 6: Shape functions associated to the composite element e_{12}. From left to right and top to bottom: Individual shape functions associated to nodes C, B, A, P_2, P_1 and five shape functions superimposed on the element.

By mean of condition (8), the dof associated to the hanging node can be eliminated, defining new shape functions $\widehat{\mathbf{N}}^{\mathbf{P1}}$ and $\widehat{\mathbf{N}}^{\mathbf{P2}}$ associated to the parent nodes:

$$\widehat{\mathbf{N}}^{\mathbf{P_1}} = \mathbf{N}^{\mathbf{4}}_{\mathbf{e_2}} + \frac{1}{2}\left(\mathbf{N}^{\mathbf{4}}_{\mathbf{e_1}} + \mathbf{N}^{\mathbf{1}}_{\mathbf{e_2}}\right) \tag{11}$$

$$\widehat{\mathbf{N}}^{\mathbf{P_2}} = \mathbf{N}^{\mathbf{1}}_{\mathbf{e_1}} + \frac{1}{2}\left(\mathbf{N}^{\mathbf{4}}_{\mathbf{e_1}} + \mathbf{N}^{\mathbf{1}}_{\mathbf{e_2}}\right) \tag{12}$$

Now, elements e_1 and e_2 can be considered as a unique composite finite element e_{12} with five nodes (the hanging node was condensed at the composite element level). The shape functions corresponding to this new element are depicted in figure 6. Thanks to this alternative way for writing the one half constraint on the dofs, continuity along edge P_1P_2 and partition of unity are automatically ensured. These new shape functions are considered in the context of the X-FEM in the next section. Finally, note that shape

functions N^A, N^B and N^C of the composite element exhibit a discontinuous gradient. This can be overcome by integrating the weak form separately on elements e_1 and e_2. This approach, based on replacing a shape function by linear combination of master shape functions is similar to the one proposed by Sukumar and Pask [38] in the context of periodic boundary conditions. The authors proposed to enforce periodic and Bloch-periodic conditions by mean of the replacement of a set of Neumann shape functions by a linear combination of the other shape functions. Two approaches were proposed to apply this condition in practice: either by enforcing the linear combination during the assembly, or after the assembly by row/column matrix operations and deletions. In this paper, the former approach was considered due to its simple implementation within our X-FEM code. However, the latter could also bee applied.

5.2. The X-FEM case

The case of enriched approximations is now considered. Figure 7(a) depicts such a case. If elements e_1 and e_2 are considered as a unique element e_{12} that verifies the

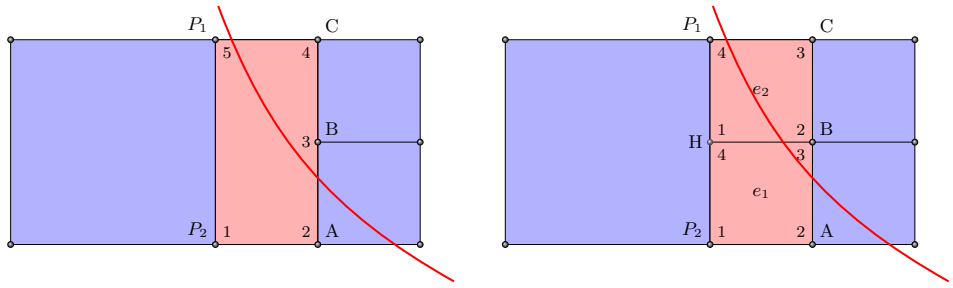

Figure 7: Enriched hanging node. (a) Composite element; (b) Two classical finite elements plus hanging node.

partition of unity, the approximation can be enriched following the approach presented in section 4. The only difference stems from the fact that the supports of the shaped functions associated to the parent nodes P_1 and P_2 extend on both element e_1 and e_2 (see figure 7(a)). The enrichment of the approximation is now trivial as the hanging node was eliminated from the approximation. However for practical purpose, we would like to treat the composite element as two elements with classical shape functions (see figure 7(b)). This is why the implementation of the strategy described above is done as follows:

1. Select the enriched degrees of freedom based on the composite element e_{12} (see figure 7(a)).

2. Consider the composite element as two classical finite elements (see figure 7(b)) with a proper constraint on the dofs for the assembly process.

Considering the composite element as two classical finite elements plus additional constraints on the hanging dofs enables minimal modifications in the finite element code: no special elements have to be considered in the assembly. Thus, no special mapping has to be defined in order to map the composite parent element on the physical one: this makes the extension of this approach to the 3D setting straightforward as there is no need to use different composite elements depending on the number of hanging nodes on an element (unlike [37]). Note also that this approach can still be applied if the elements of the mesh are converted to simplicies.

After enriching the composite element, the approximation is written as:

$$\mathbf{T}(\mathbf{x})|_{\Omega_{e_1}\cup\Omega_{e_2}} = \sum_{\alpha=1}^{5} \mathbf{N}^{\alpha}\ T^{\alpha} + \sum_{\alpha=1}^{5} \mathbf{N}^{\alpha}\ \left(\sum_{\beta=1}^{n_e} a_{\beta}^{\alpha}\ \phi_{\beta}(\mathbf{x})\right) \tag{13}$$

The shape functions associated to the parent nodes can be re-expressed in term of the shape function of the hanging node (equations (11) and (12)), then separated on their initial element. Thus, relation (13) can be written separately on elements e_1 and e_2:

$$\begin{aligned}\mathbf{T}(\mathbf{x})|_{\Omega_{e_1}\cup\Omega_{e_2}} = &\sum_{\alpha=1}^{4} \mathbf{N}_{\mathbf{e_1}}^{\alpha}\ T^{\alpha} + \sum_{\alpha=1}^{4} \mathbf{N}_{\mathbf{e_1}}^{\alpha}\ \left(\sum_{\beta=1}^{n_e} a_{\beta}^{\alpha}\ \phi_{\beta}(\mathbf{x})\right) \\ &+ \sum_{\alpha=1}^{4} \mathbf{N}_{\mathbf{e_2}}^{\alpha}\ T^{\alpha} + \sum_{\alpha=1}^{4} \mathbf{N}_{\mathbf{e_2}}^{\alpha}\ \left(\sum_{\beta=1}^{n_e} a_{\beta}^{\alpha}\ \phi_{\beta}(\mathbf{x})\right)\end{aligned} \tag{14}$$

where:

$$T^{H} = \frac{1}{2}\left(T^{P_1} + T^{P_2}\right) \tag{15}$$

$$a_{\beta}^{H} = \frac{1}{2}\left(a_{\beta}^{P_1} + a_{\beta}^{P_2}\right) \tag{16}$$

This shows that the only special treatment that is needed for hanging nodes in the case of X-FEM is to constrain their value to one half of the parents nodes, for both classical and enriched dofs. In fact, one additional requirement has to be taken into account to make this approach work in all cases. Consider the continuity of the interpolated field across edge P_1P_2: On the coarse element side, the approximation is:

$$\mathbf{T}(\mathbf{x})|_{\Omega_e} = \mathbf{N}^{\mathbf{P_1}}\ T^{P_1} + \mathbf{N}^{\mathbf{P_2}}\ T^{P_2} + \mathbf{N}^{\mathbf{P_1}}\ \left(\sum_{\beta=1}^{n_e} a_{\beta}^{P_1}\ \phi_{\beta}(\mathbf{x})\right) + \mathbf{N}^{\mathbf{P_2}}\ \left(\sum_{\beta=1}^{n_e} a_{\beta}^{P_2}\ \phi_{\beta}(\mathbf{x})\right) \tag{17}$$

On the fine side, the approximation is:

$$\mathbf{T}(\mathbf{x})|_{\Omega_e} = \widetilde{\mathbf{N}}^{\mathbf{P_1}}\, T^{P_1} + \widetilde{\mathbf{N}}^{\mathbf{P_2}}\, T^{P_2} + \widetilde{\mathbf{N}}^{\mathbf{H}}\, T^{H} + \\ + \widetilde{\mathbf{N}}^{\mathbf{P_1}} \left(\sum_{\beta=1}^{n_e} a_\beta^{P_1}\, \phi_\beta(\mathbf{x}) \right) + \widetilde{\mathbf{N}}^{\mathbf{P_2}} \left(\sum_{\beta=1}^{n_e} a_\beta^{P_2}\, \phi_\beta(\mathbf{x}) \right) + \widetilde{\mathbf{N}}^{\mathbf{H}} \left(\sum_{\beta=1}^{n_e} a_\beta^{H}\, \phi_\beta(\mathbf{x}) \right) \tag{18}$$

Where $\widetilde{N}$ (resp N) stands for the shape functions associated to the fine (resp coarse) elements: $\widetilde{N}^i = N^i_{e_1}$ on element e_1 and $\widetilde{N}^i = N^i_{e_2}$ on element e_2. Writing the continuity of the field across the hanging edge requires equality between eqns (17) and (18). This condition can be split in two sets of equations: One related to the classical part of the approximation and one related to the enriched one:

$$\mathbf{N}^{\mathbf{P_1}}\, T^{P_1} + \mathbf{N}^{\mathbf{P_2}}\, T^{P_2} = \widetilde{\mathbf{N}}^{\mathbf{P_1}}\, T^{P_1} + \widetilde{\mathbf{N}}^{\mathbf{P_2}}\, T^{P_2} + \widetilde{\mathbf{N}}^{\mathbf{H}}\, T^{H} \tag{19}$$

$$\phi_\beta(\mathbf{x}) \left(\mathbf{N}^{\mathbf{P_1}} a_\beta^{P_1} + \mathbf{N}^{\mathbf{P_2}} a_\beta^{P_2} \right) = \phi_\beta(\mathbf{x}) \left(\widetilde{\mathbf{N}}^{\mathbf{P_1}} a_\beta^{P_1} + \widetilde{\mathbf{N}}^{\mathbf{P_2}}\, a_\beta^{P_2} + \widetilde{\mathbf{N}}^{\mathbf{H}} a_\beta^{H} \right) \tag{20}$$

where equation (20) must be written for $\beta = 1 \cdots n_e$. Equation (19) is automatically verified, thanks to constraint (15). Thus, continuity will be ensured across edge P_1P_2 if equation (20) is verified. One can notice that both lhs and rhs of this equation are in fact equation (19) times $\phi_\beta(\mathbf{x})$. Thus, it will be also automatically verified thanks to condition (16) provided that $\phi_\beta(\mathbf{x})$ is continuous across edge P_1P_2. This is true for the majority of classical enrichment functions used in the literature (voids [18], fracture mechanics [7]), but not in the case of material interfaces treated by the ridge function, as the support of the ridge is different in the coarse and in the fine elements (see figure 8). This has an impact on the way material interfaces are taken into account: this aspect is thus considered separately in the following section.

5.3. The case of Material Interfaces

As stated above, the ridge enrichment is not continuous across the hanging edge (see figure 8), and the methodology presented above cannot be applied. Multiple possibilities could be considered to deal with this issue. First, the classical "abs" enrichment function [18] could be considered. In this case, the continuity of the enrichment function is ensured across edge P_1P_2 as the support of the function is not compact. However, it has been observed that the convergence rate with this function is not optimal [18, 19]. One can overcome this issue with the use of the so-called "corrected X-FEM" approximation from Fries [20]. One could also define the enrichment function independently of the mesh. This solution would allow the construction of a continuous enrichment function across P_1P_2, but would also lead to difficulties in the integration of the weak form if it exhibits gradient discontinuities inside the finite elements (not only on the interface).
In the case of the ridge function, one could extend the support of the ridge so that it is continuous along edge P_1P_2, like in [42]. However, the choice on the size of the support should evolve along the interface depending on the size of edge P_1P_2 (this

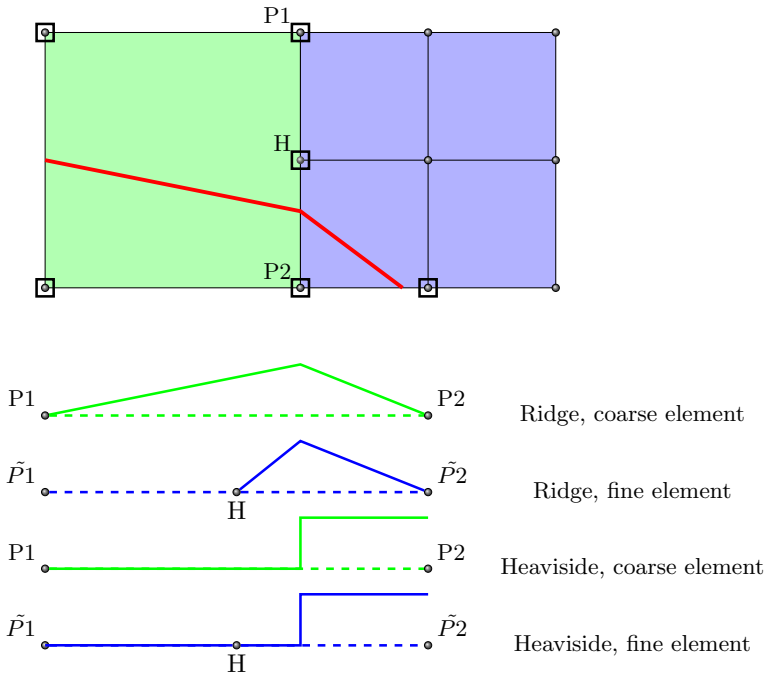

Figure 8: The case of material interfaces.

size must be at least the distance P_1P_2): This issue should lead to difficulties in 3D. Alternatively, one could define a ridge function that is built by mean of the composite shape functions: this approach would lead to a a continuous ridge function across edge P_1P_2. This last approach is illustrated in appendix A, but was not considered hereunder: We rather follow an alternative path which has drawn a lot of attention lately: the approximation is made discontinuous across the material interface by mean of a Heaviside enrichment, then it is "glued" to ensure continuity a posteriori. The Heaviside function is continuous across P_1P_2, which means that the strategy presented in section 5 can be applied. However, imposing the continuity is not an easy task: penalty can be considered, but the approach is not consistent so that the penalty parameter has to tend to infinity with mesh refinement. Moreover the value of this parameter is user dependent. The most rigorous approach consists in the use of Lagrange multipliers along the interface. Lot of work has been published lately on this topic [23, 24, 43, 25, 44], which shows that the choice of the proper Lagrange multipliers space is a complex issue. Here, there is an additional complexity because of hanging nodes. This is why we will focus on the use of the Nitsche approach which can be seen as a consistent form of the penalty approach [45, 46], or as a stabilized Lagrange multipliers approach [47]. Here, we follow [46] to write the gluing along the interface. In the following, Γ denotes the interface between the two materials and $[\![T]\!]$ denotes the jump in the approximation field (which has to vanish). Furthermore, $< \bullet >$ stands for the mean of $\bullet$ across Γ. The Nitsche approach

introduces a parameter β in order to impose the condition along Γ. The formulation of the problem is written as:

$$\begin{aligned}\int_\Omega \lambda\, \boldsymbol{\nabla} T \cdot \boldsymbol{\nabla} T^*\, d\Omega + \int_\Gamma \beta [\![T]\!][\![T^*]\!]\, d\Gamma \\ - \int_\Gamma [\![T]\!] < \lambda\, \boldsymbol{\nabla} T^* \cdot \mathbf{n} >\, d\Gamma \\ - \int_\Gamma < \lambda\, \boldsymbol{\nabla} T \cdot \mathbf{n} > [\![T^*]\!]\, d\Gamma \\ = \int_{\partial\Omega_N} g T^*\, d\Gamma \quad \forall T^* \in H_0^1(\Omega)\end{aligned} \tag{21}$$

With this approach, β must be chosen in order to ensure the coercivity of the bilinear form. It is also possible to obtain the limit value for β that ensures stability by mean of a global eigenvalue problem proposed by Griebel [48], or a local one proposed by Embar et al. [49]. In the following, β will be set to a given value that ensures the stability of the approach.

6. NUMERICAL EXAMPLES

In this section, numerical examples are proposed in order to validate the approach. The validation will be carried out by mean of error driven mesh adaptation, with known analytical solution. The adaptation will be driven by the exact relative error (defined by equation (22)), imposing refinement when the error within an element exceed a given threshold.

$$\varepsilon_{\Omega_e} = \sqrt{\frac{\int_{\Omega_e} (\boldsymbol{\nabla} T - \boldsymbol{\nabla} T^{ex}) \lambda (\boldsymbol{\nabla} T - \boldsymbol{\nabla} T^{ex})\, d\Omega}{\int_\Omega \boldsymbol{\nabla} T^{ex} \lambda \boldsymbol{\nabla} T^{ex}\, d\Omega}} \tag{22}$$

This approach does not lead to optimal meshes in term of error distribution, but is sufficient to validate the approach. In practice, the adapted mesh is monitored in order to check that the error does not localize near the hanging nodes. Moreover, the adaptation process is compared to results obtained by a mesh modification approach that eliminates the hanging nodes (see figure 2). Finally, note that in the following each active cell of the quadtree is split into two triangular elements to build a simplex mesh.

6.1. Holes

Consider a $[-1, 1] \times [-1, 1]$ plane domain containing a hole at its center with a radius $R = 0.4$ (see fig.9). The external boundaries are submitted to Neumann boundary conditions and the hole is free. The domain is submitted to an internal heat source such that the exact solution is:

$$T(r, \theta) = e^{-(R-r)^2} \sin(\theta) \tag{23}$$

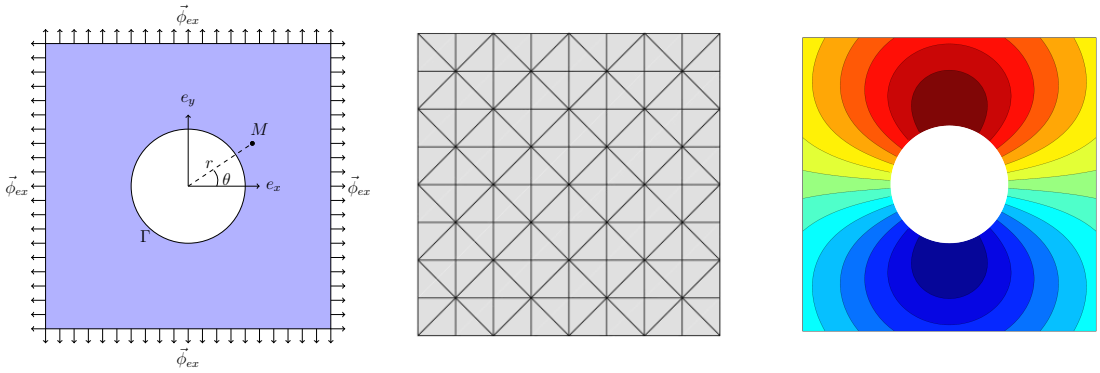

Figure 9: Geometry, initial mesh and solution for the hole's example

The initial mesh is built from a level 3 quadtree grid ($8 \times 8 \times 2$ elements, see figure 9). The maximum error contribution allowed is fixed to 5.10^{-4}. The procedure is run until none of the elements needs to be refined. The final meshes with and without hanging node are given in figure 10.

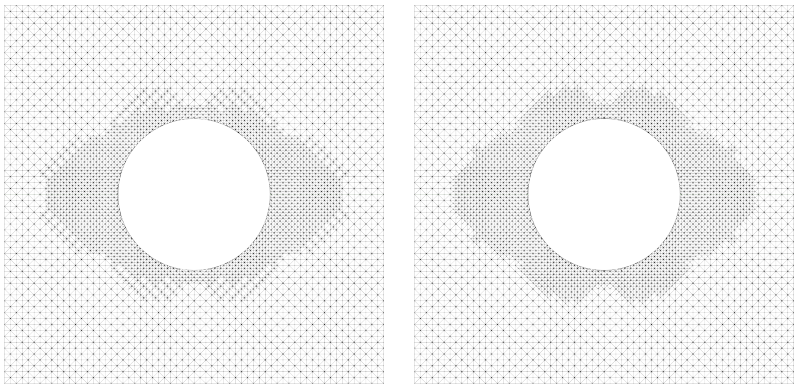

Hanging nodes No hanging nodes

Figure 10: Final mesh after adaptation

In both cases, the refinement stabilizes after some iterations. No focus of refinement is observed around the enriched elements. The final meshes are nearly the same, which validates the method. Moreover, the error distribution is also similar (see fig.11), even if it is smoother without hanging nodes because of the smoother gradation of the mesh size. We remark also that the computation with hanging nodes needs more iterations to meet the tolerance (8 iterations versus 5 without hanging nodes). In fact, when hanging nodes are considered, iterations 6, 7 and 8 only affect classical elements away from the hole. This stems from the difference of size between two neighbors with different level which makes them sensitive to pollution errors and extend the refinement on some isolated elements.

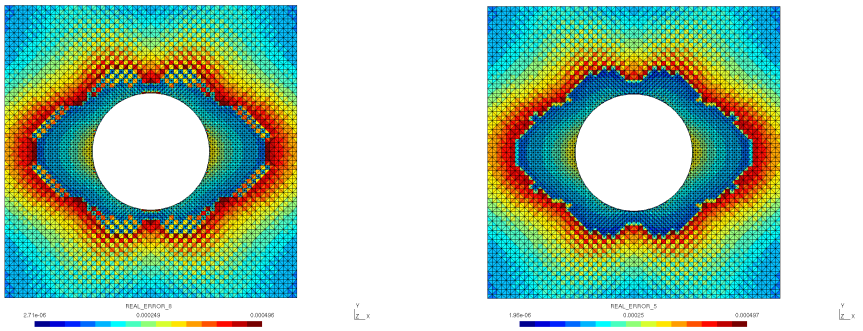

Hanging nodes No hanging nodes

Figure 11: Error distribution

6.2. Singular field

Consider a $[-1,1] \times [-1,1]$ plane domain containing a singularity at its center (see figure 12). The analytical solution of this problem is:

$$T(r,\theta) = \sqrt{r}\sin(\theta/2) \tag{24}$$

The solution is singular near the center of the domain, and discontinuous along the line $(-1,0)-(0,0)$. The X-FEM approximation is enriched with the Heaviside function for the nodes whose support is crossed by the discontinuity line, and with a near-tip asymptotic function $\sqrt{r}\sin(\theta/2)$ for nodes whose support contains the center of the domain.

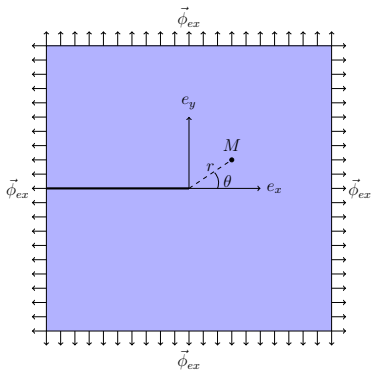

Figure 12: Singular field example

The process begin with a mesh composed of 128 elements of level 3, and the threshold for refinement is set to 1.10^{-3} for the relative error. First, a mesh with center at $(0,0)$ is considered. The final mesh is given in figure 13. It took ten adaptations to obtain this mesh both with or without hanging nodes. It can be seen that the refinement level is the same for the two approaches which validates the proposed approach in this

case: no localization of the error was observed, and a close-up is necessary to see some discrepancy between the two solutions (see figure 14). Concerning the error distribution, it is consistent between the two approaches, even if it is smoother without hanging nodes, thanks to a smoother mesh gradation (see figure 15). Remark that when using a geometrical enrichment of radius 0.2 (see [50, 51]), only 5 iterations were necessary to get an error below the 1.10^{-3} threshold.

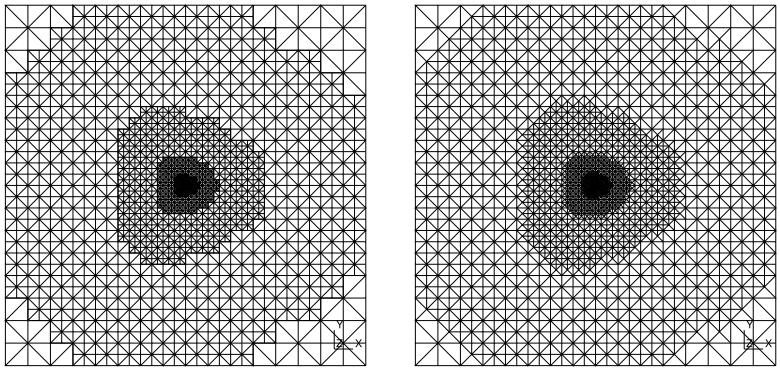

Hanging nodes No hanging nodes

Figure 13: Final mesh after adaptation

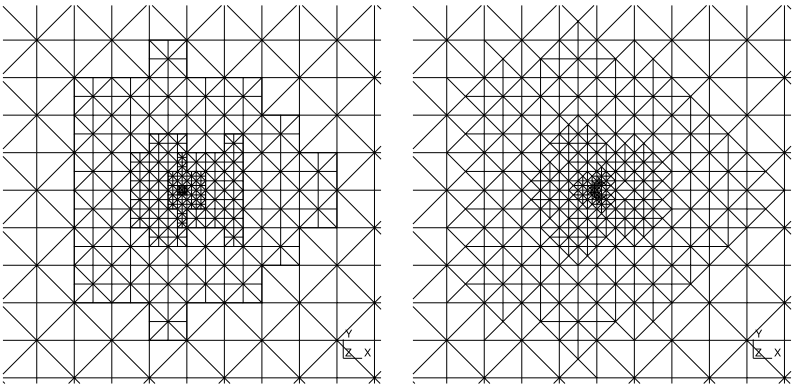

Hanging nodes No hanging nodes

Figure 14: Final mesh after adaptation (zoom near the singularity)

The case of an non-centered domain is now considered. The domain bounding box is now $[-1.1, 0.9] \times [-1.1, 0.9]$, which enables the discontinuity to cross the elements. A geometrical near-tip enrichment of radius 0.2 is considered, and exact fluxes are imposed on the boundaries. The conclusions are similar to those of the centered mesh. One can also remark some orphan refinement areas in figure 17 for the mesh with hanging nodes, but also for the mesh without hanging nodes. The error distribution is presented in figure 18 and is similar in the two cases. Finally, note that it took 7 iterations to the

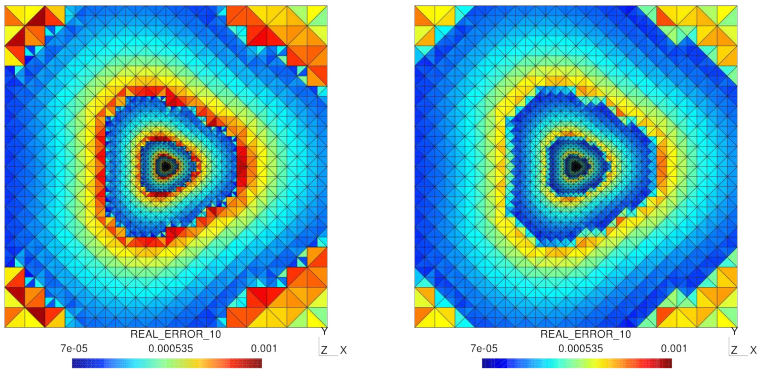

Hanging nodes No hanging nodes

Figure 15: Final error after adaptation

process to meet the 1.10^{-3} relative error tolerance in this case (with and without hanging nodes).

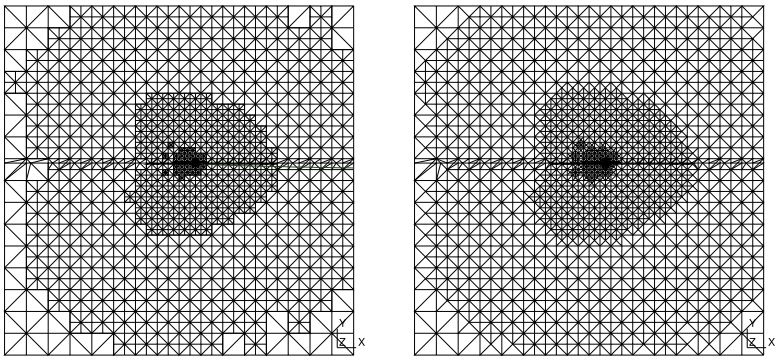

Hanging nodes No hanging nodes

Figure 16: Final mesh after adaptation (shifted case). The iso-zero and subelements of the plane defining the singularity are shown.

6.3. Material Interfaces

Consider a $[-1, 1] \times [-1, 1]$ plane domain that contains a circular inclusion of radius $a = 0.7$ at its center (see figure 19). The thermal conductivity of the matrix is set to 1.0, whereas it is set to 10.0 for the inclusion. The analytical solution of this problem is given by the following expression:

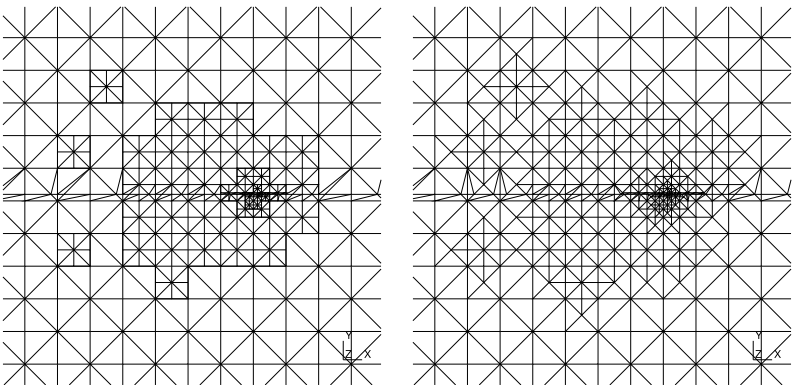

Hanging nodes No hanging nodes

Figure 17: Final mesh after adaptation (shifted case, zoom near the singularity). The iso-zero and subelements of the plane defining the singularity are shown.

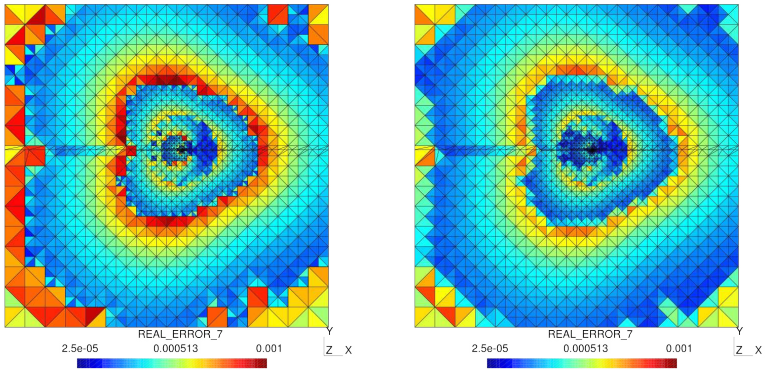

Hanging nodes No hanging nodes

Figure 18: Final error after adaptation (shifted case). The iso-zero and subelements of the plane defining the singularity are shown.

$$T(r,\theta) = r^2 \quad \text{for } r < 0.4 \tag{25}$$

$$T(r,\theta) = \frac{5r^3a^2 - 4r^2a^2 - 10r^2a^3 + r^2 + 9ra^3 + 5ra^4 - 2ra + a^2}{5a^2} \quad \text{otherwise} \tag{26}$$

The solution exhibits a discontinuity in its gradient at the material interface Γ (see figure 20). The numerical solution is obtained, as presented in section 5.3, with the use of a Nitsche parameter $\beta = 10^5$. This value was selected after a sensitivity study on the convergence rate with respect to β. The results are reported in figure 21 and show no influence of the value of β in the range $[10^3, 10^7]$.

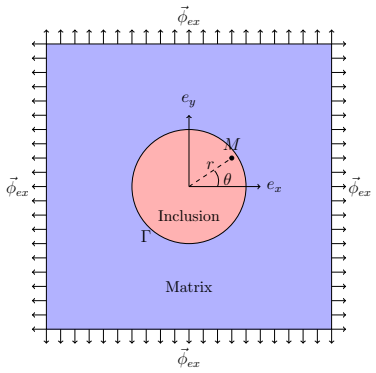

Figure 19: Bimaterial example

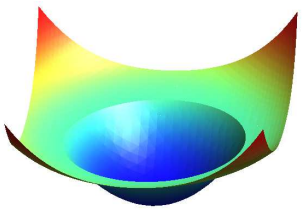

Figure 20: Bimaterial example

The error threshold is set to 1.10^{-3}, and the initial mesh is a uniform level 3 mesh. Like in the previous examples, the adapted mesh is compared with and without hanging nodes: it can be seen in figures 22 and 23 that the meshes have exactly the same shape, and it took exactly the same number of iterations to meet the error requirement (5 iterations). Concerning the error fields, they have the same shape (no error peak near the interface with hanging nodes), and the error with hanging nodes is still smoother due to a more graded mesh.

If the value of β is changed, the shape of the adapted mesh is changed, as the strength of the imposition of the continuity constraint across the interface is modified. This is why the discrepancies appear near the interface (see figure 25).

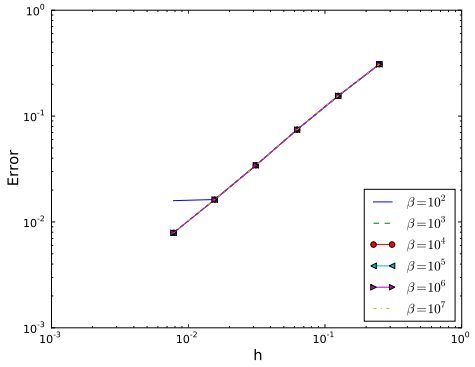

Figure 21: Influence of β on the convergence

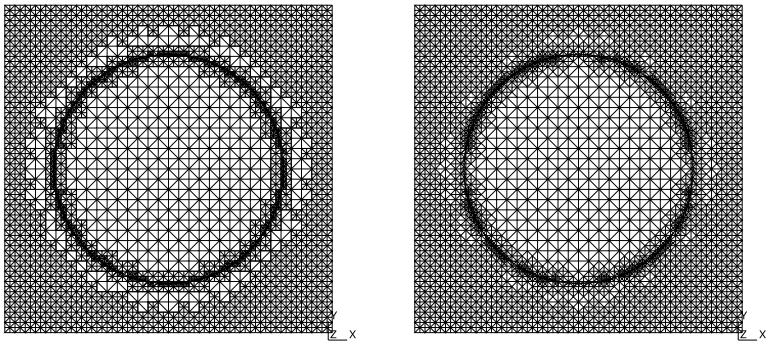

Hanging nodes No hanging nodes

Figure 22: Final mesh after adaptation

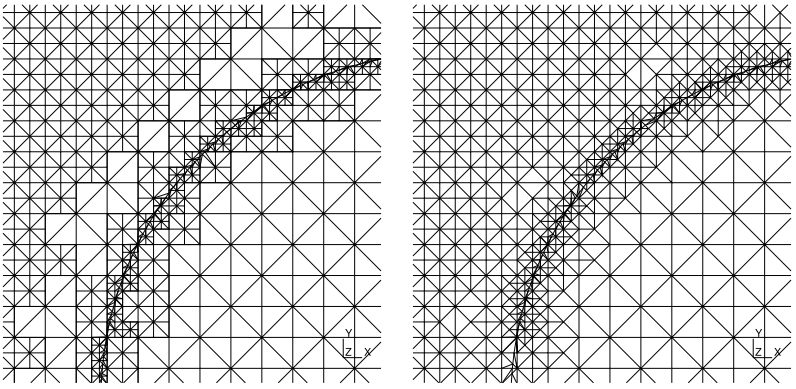

Hanging nodes No hanging nodes

Figure 23: Final mesh after adaptation (zoom near the interface)

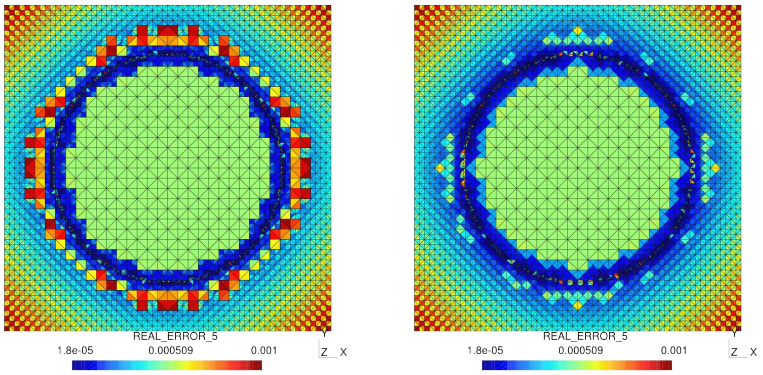

Hanging nodes No hanging nodes

Figure 24: Final error after adaptation

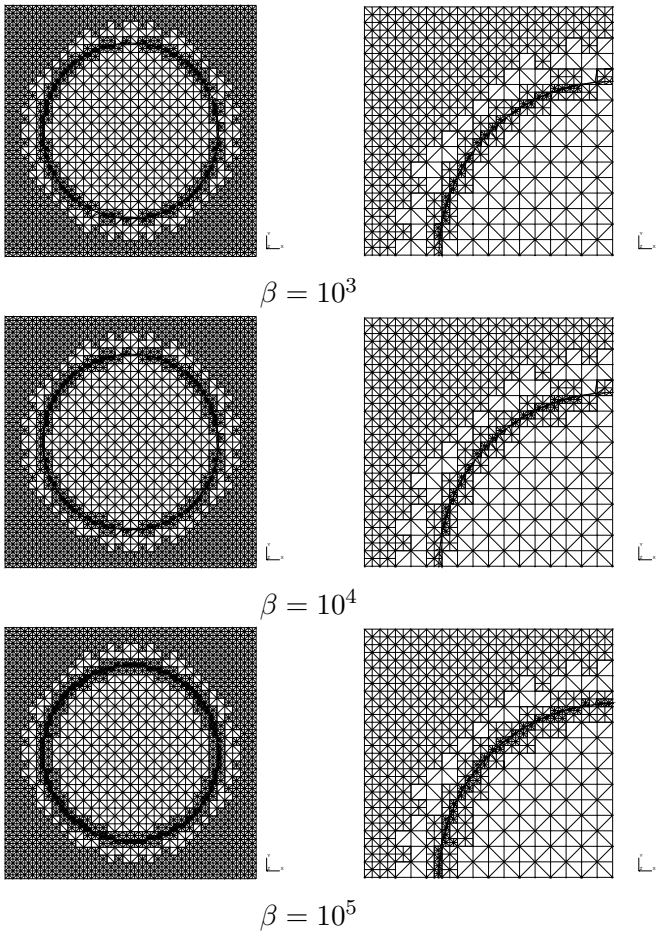

$\beta = 10^3$

$\beta = 10^4$

$\beta = 10^5$

Figure 25: Influence of β on the adapted mesh

Finally, the adaptation process is applied on a pure quadtree mesh (without splitting the quadrangles into two triangular elements) for illustrative purpose. Parameter β is still set to 10^5 (after a convergence study to monitor the influence of the parameter). It took 5 iterations to meet the 10^{-3} tolerance, like in the previous examples. The adapted mesh is depicted in figure 26: the shape of this mesh is consistent with the one obtained with simplices.

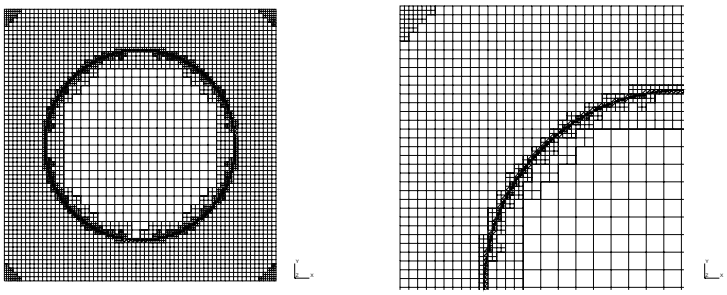

Figure 26: Final mesh after adaptation, pure quadtree case

6.4. Extention to 3D

The proposed approach can be directly applied in the 3D setting by mean of proper combination of 3D shape functions. This extension is first illustrated through simple examples that focus on the quality of the enriched field. Finally, an adaptive example is proposed. Only the case of material interfaces is addressed here, as the case of holes involves no enrichment and singularities share similar difficulties with material interfaces.

6.4.1. Quality of the enriched field

The quality of the enriched field is monitored through the example proposed in figure 27. It consists in a domain composed of two materials ($\lambda_1 = 1.0$, $\lambda_2 = 10.0$) that is subjected to imposed (and unit) external fluxes along two of its boundaries. The resulting temperature field is linear over the two parts of the domain. The exact solution is extracted from a $[2 \times 2]^3$ cube (dashed in figure 27), and applied on the boundaries of the $[2 \times 2]^3$ mesh depicted in figure 28. It can be seen on this figure that this mesh exhibits hanging nodes. Four (arbitrary) cases are considered depending on the location and the orientation of the computational domain (see figure 29). Depending on the case, hanging nodes and their parents may be naturally enriched, or enriched through the approach proposed in section 5. Moreover, the value of the enriched dofs of the parents may be constant (case 1. and case 2.) or may depend on their position (case 3. and case 4.). In all the cases, Nitsche's parameter is set du 10^5. The iso temperatures corresponding to these four cases are depicted in figure 30: It can be seen that the iso surfaces are perfectly planar, even when hanging nodes are enriched. Moreover, the error with respect to the analytical temperature field is close to machine precision (in the order of 10^{-12} - 10^{-15}), which validates the approach in 3D.

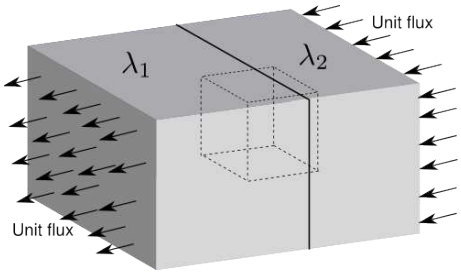

Figure 27: 3D bimaterial example (dashed cube = computational domain).

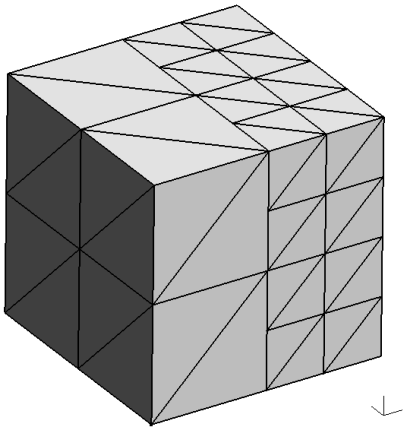

Figure 28: Computational mesh.

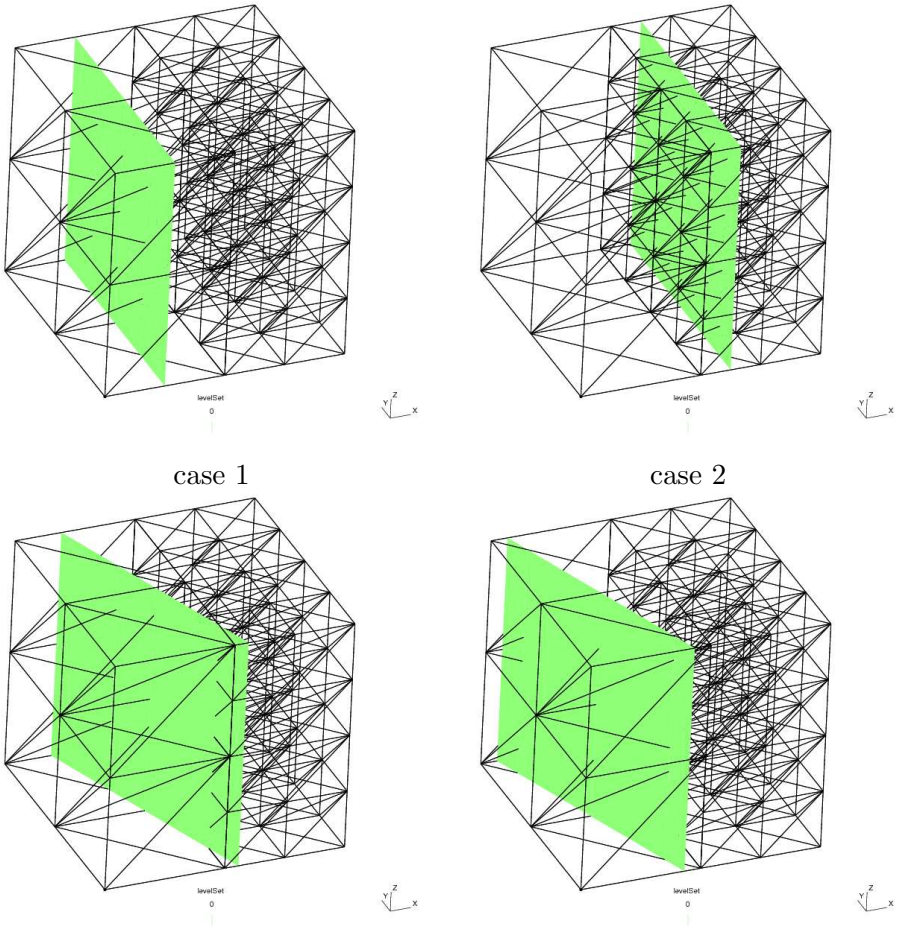

Figure 29: Four computational cases.

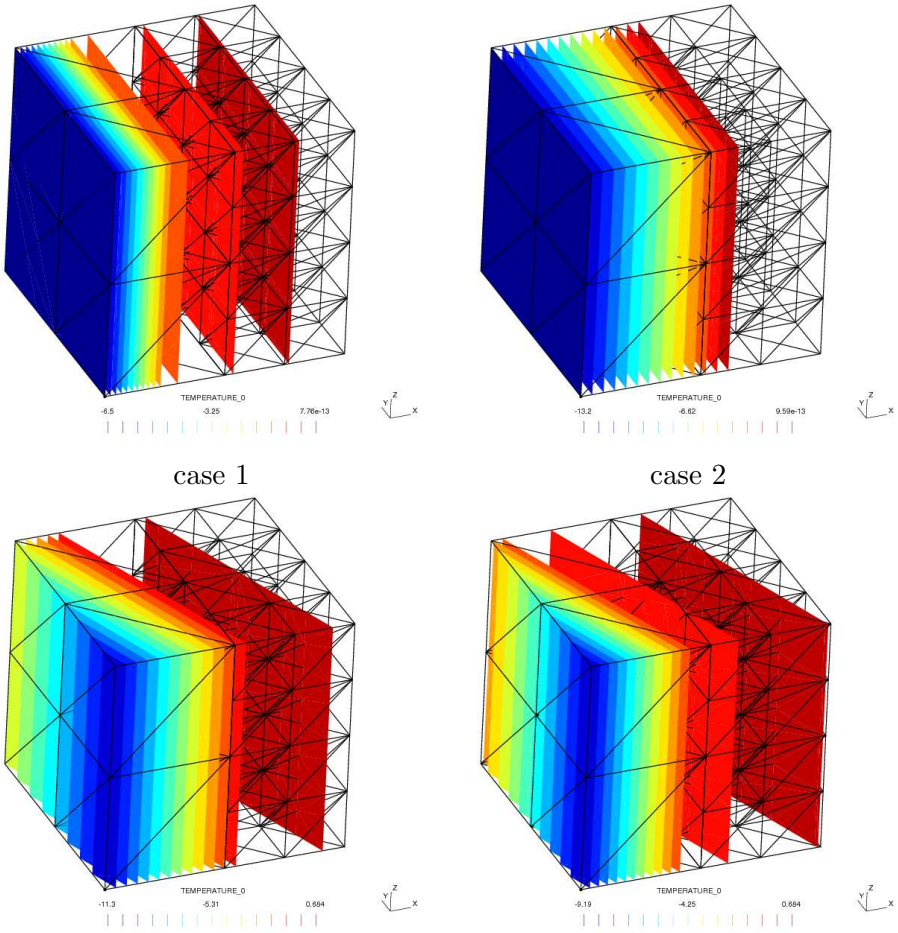

case 1 case 2

case 3 case 4

Figure 30: Computation results.

6.4.2. 3D adaptation

A 3D adaptive example is finally presented: Consider a $[2 \times 2]^3$ cube containing a spherical inclusion of radius 0.7 at its center. The thermal conductivity of the matrix is set to 1.0 whereas the conductivity of the inclusion is set to 10.0. A volume heat source is imposed in the domain so that the exact temperature takes the same expression as in section 6.3 (see equations (25) and (26)). One fourth of the domain is considered, symmetry conditions and exact fluxes are imposed on the boundaries of the mesh, whereas the temperature is prescribed to zero at the center of the inclusion. Nitsche parameter is set to 10^5, target error is set to 2.10^{-3} and 5.10^{-4} and the initial mesh is a $6 \times (8 \times 8 \times 8)$ tetrahedral mesh (level 3). For the 2.10^{-3} threshold, the adaptive process requires 5 iterations to get an acceptable solution, whereas it took 6 iterations for the 5.10^{-4} threshold. The final mesh levels are depicted in figure 31 and show no localization of the refinement near enriched hanging nodes when the threshold is decreased (see figure 32). The final iso-temperatures for both cases are depicted in figure 33, and it can be seen that the iso-surfaces are very smooth, even near the interface (especially for the 5.10^{-4} threshold).

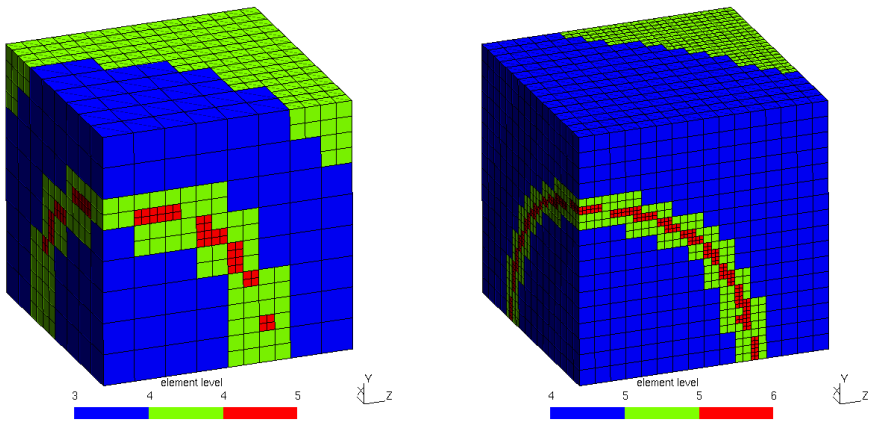

2.10^{-3} 5.10^{-4}

Figure 31: Final mesh levels

7. CONCLUSION

In this paper, we proposed a strategy to use quadtree and octree meshes in the context of partition of unity finite element methods. Rather than modifying the mesh, introducing special finite elements or using polygonal finite elements, constraining the degrees of freedom was considered. By rearranging the shape function, it was possible to define composite elements whose shape functions are enriched. Practically, the shape functions were re-expressed on the initial elements which lead to a proper definition of the constraint that has to be imposed for the hanging dofs. This approach enables to treat the

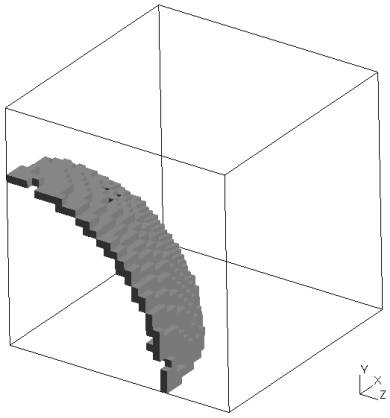

Figure 32: Finest mesh level (5.10^{-4} threshold)

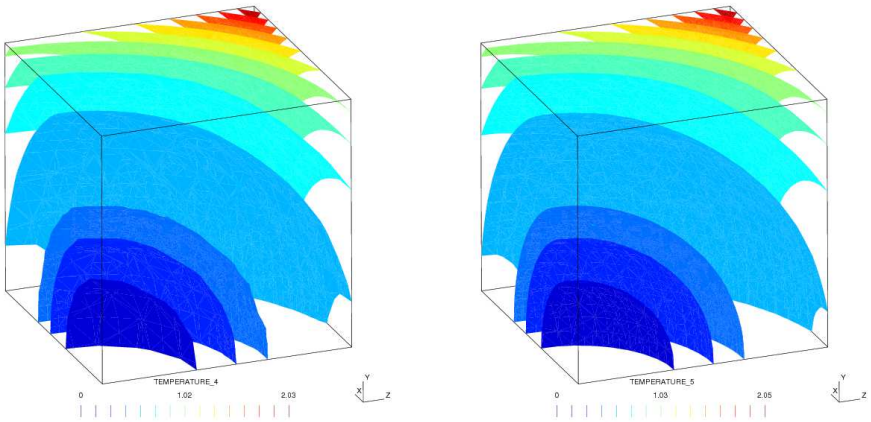

2.10^{-3} 5.10^{-4}

Figure 33: Iso-temperatures for final meshes

composite element as a classical element, which makes the use of this approach straightforward, even in the 3D setting. The condition that is obtained for the enriched hanging dofs shares similar features with the projection operator proposed by Rannou et al. [52] in the context of extended multigrid methods. However, in [52] the operator was based on a collocation approach. On the contrary, exact continuity along the hanging edges is obtained here. Moreover, we tackled the case of incompatible enrichment which introduced high order error in [52]. The proposed approach was validated in the case of holes, material inclusions and singularities in both 2D and 3D. An alternative approach was proposed in the case of material interfaces to be able to use the proposed strategy. This approach is based on a discontinuous approximation across the material interface, and the use of the Nitsche approach to make the jump in the approximated field vanish. In 2D, a comparison of the results with a mesh modification strategy showed no significant difference between the two approaches in term of final mesh, and very little differences in term of error distribution. These differences could be related to the fact that the meshes obtained with the modification strategy were more graded than the quadtree ones. In 3D, the analytical solution of a simple problem could be recovered, even with enriched hanging nodes, and the results obtained on a fully 3D examples exhibited very smooth solutions and consistent refinement pattern.

A. CONSTRAINED RIDGE FUNCTION FOR QUADTREE/OCTREE MESHES

As explained in section 5.3, one possible approach to deal with the continuity issue of the ridge enrichment function across edge P_1P_2 (see figures 8 and 37 for notations) consists in writing its definition in term of the composite shape functions. Recall the expression of the ridge enrichment function:

$$R(\mathbf{x}) = \sum_{\alpha} |\phi^{\alpha}| N^{\alpha}(\mathbf{x}) - \left| \sum_{\alpha} \phi^{\alpha} N^{\alpha}(\mathbf{x}) \right| \tag{27}$$

where ϕ_i is the signed-distance function to the interface evaluated at the vertex of node i. Rather than writing this expression on elements e_1 and e_2 separately, we choose to write it on the corresponding composite element. Thanks to this approach, $R(\mathbf{x})$ is now continuous across edge P_1P_2. Like in the remaining of the paper, this condition is considered practically as taking ϕ^H as $1/2(\phi^{P_1} + \phi^{P_2})$, and $|\phi^H|$ as $1/2(|\phi^{P_1}| + |\phi^{P_2}|)$ in the equation above. The resulting function is illustrated in the case of a bimaterial square depicted in figure 34(a). The square is made of two materials with different conductivities: 10 for the upper phase and 1 for the other one. A unit flux is imposed on the top and bottom faces of the mesh, which leads to a piecewise linear solution. The classical ridge function is depicted in figure 34(b) and exhibits a discontinuity along the hanging edges. In contrast, the "constrained" ridge function remains continuous over the domain. The solution of this problem is depicted in figure 35: One can check that the exact solution was recovered.

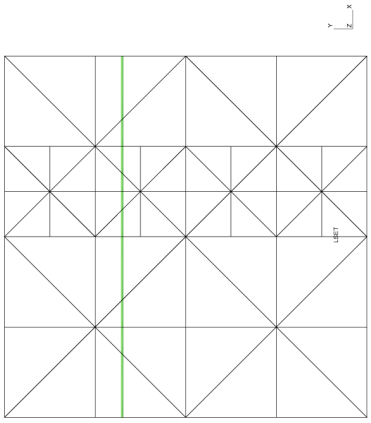

(a)

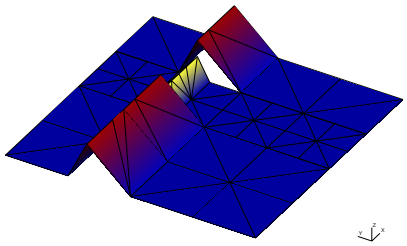

(b)

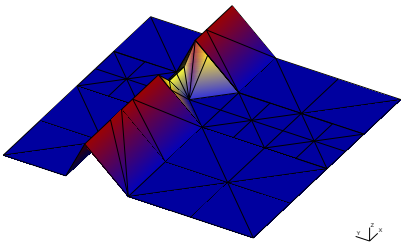

(c)

Figure 34: Simple bimaterial example: (a) Mesh and interface location. (b) Classical ridge function and (c) "Constrained" ridge function.

Finally, this "constrained" ridge function is applied in the bimaterial case presented in section 6.3. It took 5 iterations to meet the error threshold, and the corresponding adapted mesh shown in figure 36 is consistent with the one obtained using Nitsche's method (see figure 22).

B. ILLUSTRATION OF THE PROPOSED APPROACH WITH MORE THAN ONE HANGING NODE

The proposed approach is illustrated in the case where more than one hanging node appears (see figures 37 and 38). In this case, new composite shape functions associated to the composite element are naturally constructed. The shape functions that are built from linear combination of the shape functions of the original elements (e_1, e_2, e_3 and e_4) are depicted in figures 39 and 40 for the two cases of two and three hanging nodes.

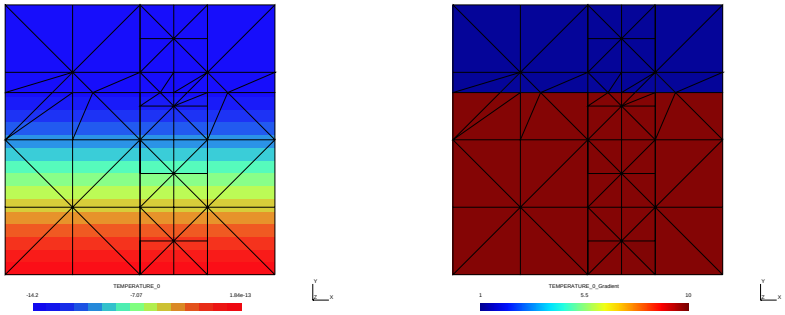

(a) (b)

Figure 35: Simple bimaterial example: (a) Temperature field and (b) Gradient field.

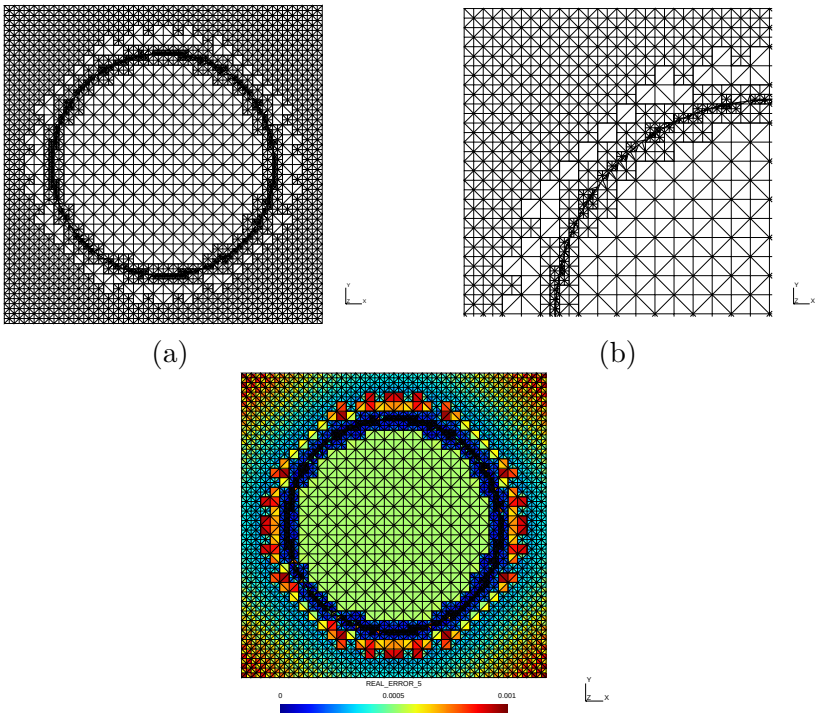

(a) (b)

(c)

Figure 36: Circular inclusion example: (a) - (b) Adapted mesh and (c) Final error distribution.

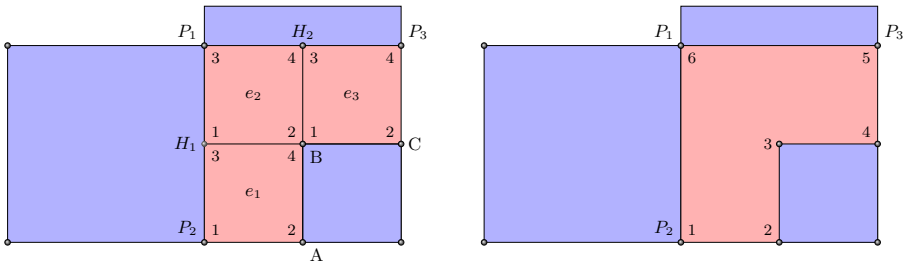

(a) (b)

Figure 37: (a) case with two hanging nodes H_1 and H_2; (b) composite elements obtained by combining the shape functions

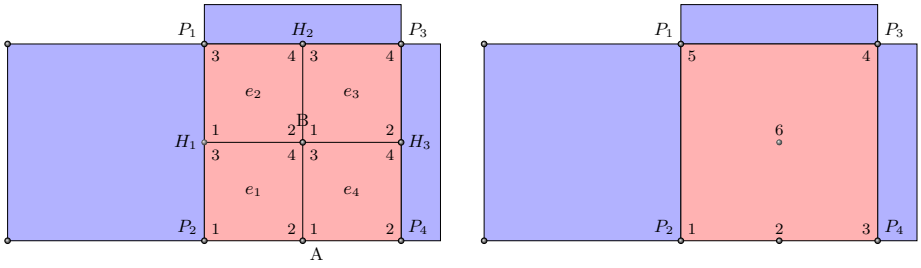

(a) (b)

Figure 38: (a) case with three hanging nodes H_1, H_2 and H_3; (b) composite elements obtained by combining the shape functions

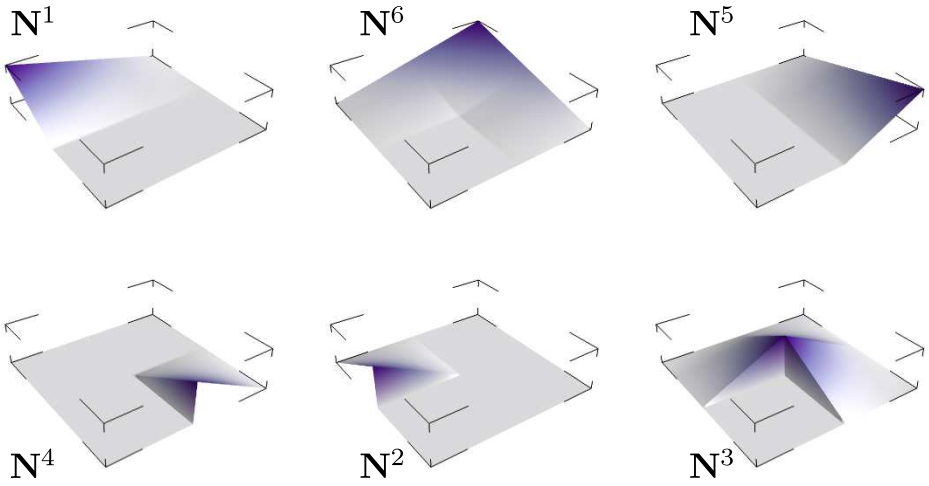

Figure 39: Shape functions associated to the composite element e_{123}.

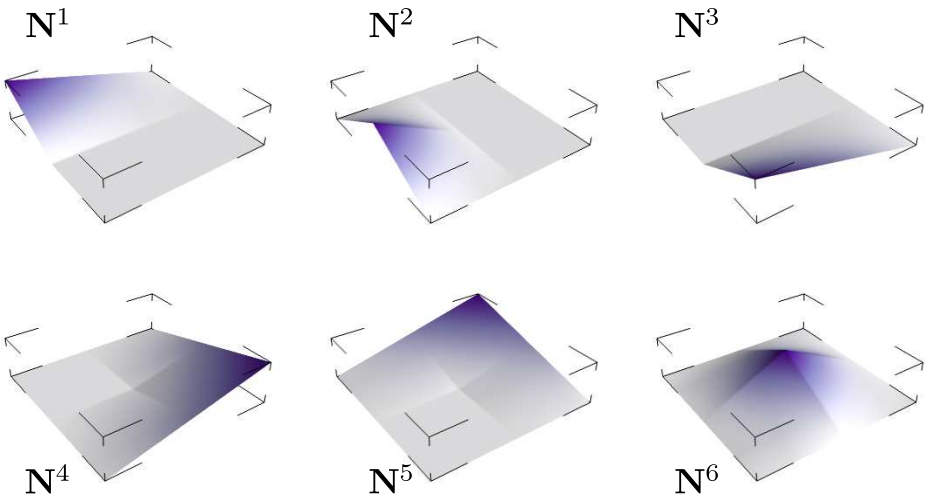

Figure 40: Shape functions associated to the composite element e_{1234}.

References

[1] I. Babuska and J. Y. Melenk. The partition of unity finite element method. *International Journal for Numerical Methods in Engineering*, 40(4):727–758, 1997.

[2] P. Frey and P. George. *Mesh Generation: Application to Finite Elements*. 2000.

[3] Mark Ainsworth and Bill Senior. Aspects of an adaptive hp-finite element method: Adaptive strategy, conforming approximation and efficient solvers. *Computer Methods in Applied Mechanics and Engineering*, 150(1-4):65–87, 1997.

[4] Petr Krysl, Eitan Grinspun, and Peter Schrder. Natural hierarchical refinement for finite element methods. *International Journal for Numerical Methods in Engineering*, 56(8):1109–1124, 2003.

[5] Pavel Kagan, Anath Fischer, and Pinhas Z. Bar-Yoseph. Mechanically based models: Adaptive refinement for b-spline finite element. *International Journal for Numerical Methods in Engineering*, 57(8):1145–1175, 2003.

[6] A. Tabarraei and N. Sukumar. Adaptive computations using material forces and residual-based error estimators on quadtree meshes. *Computer Methods in Applied Mechanics and Engineering*, 196(25-28):2657–2680, 2007.

[7] N. Moës, J. Dolbow, and T. Belytschko. A finite element method for crack growth without remeshing. *International Journal for Numerical Methods in Engineering*, 46:131–150, 1999.

[8] T. Strouboulis, I. Babuška, and K. Copps. The design and analysis of the generalized finite element method. *Computer Methods in Applied Mechanics and Engineering*, 181:43–69, 2000.

[9] M. Stolarska, D. L. Chopp, N. Moës, and T. Belytschko. Modelling Crack Growth by Level Sets and the Extended Finite Element Method. *International Journal for Numerical Methods in Engineering*, 51(8):943–960, 2001.

[10] A. Gravouil, N. Moës, and T. Belytschko. Non-planar 3D crack growth by the extended finite element and level sets. Part II: level set update. *International Journal for Numerical Methods in Engineering*, 53:2569–2586, 2002.

[11] N. Moës, A. Gravouil, and T. Belytschko. Non-planar 3D crack growth by the extended finite element and level sets. Part I: Mechanical model. *International Journal for Numerical Methods in Engineering*, 53:2549–2568, 2002.

[12] G. Legrain, N. Moës, and E. Verron. Robust and direct evaluation of j_2 in linear elastic fracture mechanics with the x-fem. *International Journal for Numerical Methods in Engineering*, 76(10):1471–1488, 2008.

[13] J. Dolbow, N. Moës, and T. Belytschko. An extended finite element method for modeling crack growth with frictional contact. *Comp. Meth. in Applied Mech. and Engrg.*, 190:6825–6846, 2001.

[14] P. M. A. Areias and T. Belytschko. Analysis of three-dimensional crack initiation and propagation using the extended finite element method. *International Journal for Numerical Methods in Engineering*, 63(5):760–788, 2005.

[15] G. Legrain, N. Moës, and A. Huerta. Stability of incompressible formulations enriched with X-FEM. *Computer Methods in Applied Mechanics and Engineering*, 197(21-24):1835–1849, 2008.

[16] N. Moës and T. Belytschko. Extended Finite Element Method for Cohesive Crack Growth. *Engineering Fracture Mechanics*, 69:813–834, 2002.

[17] G.N. Wells, R. de Borst, and L.J. Sluys. A consistent geometrically non-linear approach for delamination. *international journal for numerical methods in engineering*, 54:1333–1355, 2002.

[18] N. Sukumar, D. L. Chopp, N. Moës, and T. Belytschko. Modeling Holes and Inclusions by Level Sets in the Extended Finite Element Method. *Comp. Meth. in Applied Mech. and Engrg.*, 190:6183–6200, 2001.

[19] N. Moës, M. Cloirec, P. Cartraud, and J.-F. Remacle. A computational approach to handle complex microstructure geometries. *Comp. Meth. in Applied Mech. and Engrg.*, 192:3163–3177, 2003.

[20] Thomas-Peter Fries. A corrected XFEM approximation without problems in blending elements. *International Journal for Numerical Methods in Engineering*, 75(5):503–532, 2008.

[21] G.J. Wagner, N. Moës, W.K. Liu, and T. Belytschko. The Extended Finite Element Method for Stokes Flow Past Rigid Cylinders. *International Journal for Numerical Methods in Engineering*, 51:293–313, 2001.

[22] J. Chessa and T. Belytschko. An extended finite element method for two-phase fluids. *Journal of Applied Mechanics (ASME)*, 70:10–17, 2003.

[23] N. Moës, E. Béchet, and M. Tourbier. Imposing dirichlet boundary conditions in the extended finite element method. *International Journal for Numerical Methods in Engineering*, 67(12):1641–1669, 2006.

[24] E. Béchet, N. Moës, and B. Wohlmuth. A stable lagrange multiplier space for the stiff interface conditions within the extende finite element method. *International Journal for Numerical Methods in Engineering*, 78(8):931–954, 2009.

[25] Mourad H, Dolbow JE, and Harari I. A bubble-stabilized finite element method for dirichlet constraints on embedded interfaces. *International Journal for Numerical Methods in Engineering*, 69:772–793, 2007.

[26] M. Duflot and S. Bordas. A posteriori error estimation for extended finite elements by an extended global recovery. *International Journal for Numerical Methods in Engineering*, 76(8):1123–1138, 2008.

[27] S. Bordas and M. Duflot. Derivative recovery and a posteriori error estimate for extended finite elements. *Computer Methods in Applied Mechanics and Engineering*, 196(35-36):3381–3399, 2007.

[28] T. Pannachet, L. J. Sluys, and H. Askes. Error estimation and adaptivity for discontinuous failure. *International Journal for Numerical Methods in Engineering*, 78(5):528–563, 2009.

[29] J. J. Ródenas, O. A. Gonzàlez-Estrada, J. E. Tarancón, and F. J. Fuenmayor. A recovery-type error estimator for the extended finite element method based on singular+smooth stress field splitting. *International Journal for Numerical Methods in Engineering*, 76(4):545–571, 2008.

[30] J. Panetier, P. Ladevze, and L. Chamoin. Strict and effective bounds in goal-oriented error estimation applied to fracture mechanics problems solved with XFEM. *International Journal for Numerical Methods in Engineering*, 81(6):671–700, 2010.

[31] Theofanis Strouboulis, Lin Zhang, Delin Wang, and Ivo Babuka. A posteriori error estimation for generalized finite element methods. *Computer Methods in Applied Mechanics and Engineering*, 195(9-12):852–879, 2006.

[32] C. A. Duarte, I. Babuška, and J.T. Oden. Generalized finite element methods for three-dimensional structural mechanics problems. *Computers and Structures*, 77(2):215–232, 2000.

[33] T. Strouboulis, L. Zhang, and I. Babuška. Generalized finite element method using mesh-based handbooks: application to problems in domains with many voids. *Computer Methods in Applied Mechanics and Engineering*, 192(28-30):3109–3161, 2003.

[34] C. A. Duarte and D. J. Kim. Analysis and applications of a generalized finite element method with global-local enrichment functions. *Computer Methods in Applied Mechanics and Engineering*, 197:487–504, Jan 2008.

[35] A. Tabarraei and N. Sukumar. Extended finite element method on polygonal and quadtree meshes. *Computer Methods in Applied Mechanics and Engineering*, 197(5):425–438, 2008.

[36] S. Bordas and S. Natarajan. On the approximation in the smoothed finite element method (SFEM). *International Journal for Numerical Methods in Engineering*, 9999(9999):n/a, 2009.

[37] A. Alizada and T. P. Fries. Cracks and crack propagation with xfem and hanging nodes in 2d. In *IV European Conference on Computational Mechanics*, 2010.

[38] N. Sukumar and J. E. Pask. Classical and enriched finite element formulations for bloch-periodic boundary conditions. *International Journal for Numerical Methods in Engineering*, 77(8):1121–1138, 2009.

[39] M.A. Yerry and M.S. Shephard. A modified quadtree approach to finite element mesh generation. *Computer Graphics and Applications, IEEE*, 3(1):39–46, 1983.

[40] William J. Schroeder, Berk Geveci, Mathieu Malaterre, and Kitware Inc. Compatible triangulations of spatial decompositions, April 2008.

[41] C. Daux, N. Moës, J. Dolbow, N. Sukumar, and T. Belytschko. Arbitrary branched and intersecting cracks with the eXtended Finite Element Method. *International Journal for Numerical Methods in Engineering*, 48:1741–1760, 2000.

[42] A. Nouy and A. Clment. eXtended stochastic finite element method for the numerical simulation of heterogeneous m aterials with random material interfaces. *International Journal for Numerical Methods in Engineering*, pages n/a–n/a, 2010.

[43] S. Geniaut, P. Massin, and N. Moës. A stable 3D contact formulation using X-FEM. *Revue européenne de mécanique numérique*, 16(2):259 – 275, 2007.

[44] John Dolbow and Isaac Harari. An efficient finite element method for embedded interface problems. *International Journal for Numerical Methods in Engineering*, 78(2):229–252, 2009.

[45] J. Nitsche. Über ein Variationprinzip zur lösung von Dirichlet-Problem bei Verwendung von Teilräumen, die keinen Randbedingungen unterworfen sind. *Abh. Math. Sem. Univ. Hamburg*, 36:9–15, 1971.

[46] Anita Hansbo and Peter Hansbo. A finite element method for the simulation of strong and weak discontinuities in solid mechanics. *Computer Methods in Applied Mechanics and Engineering*, 193(33-35):3523–3540, August 2004.

[47] Rolf Stenberg. On some techniques for approximating boundary conditions in the finite element method. *Journal of Computational and Applied Mathematics*, 63(1-3):139–148, November 1995.

[48] M. Griebel and M.A. Schweitzer. *Geometric Analysis and Nonlinear Partial Differential Equations*, chapter A particle-partition of unity method. Part V: Boundary conditions, pages 517 – 540. Springer-Verlag, Berlin, 2002.

[49] Anand Embar, John Dolbow, and Isaac Harari. Imposing dirichlet boundary conditions with nitsche's method and spline-based finite elements. *International Journal for Numerical Methods in Engineering*, pages n/a–n/a, 2010.

[50] P. Laborde, J. Pommier, Y. Renard, and Michel Salaün. High-order extended finite element method for cracked domains. *International Journal for Numerical Methods in Engineering*, 64(3):354–381, 2005.

[51] E. Béchet, H. Minnebo, N. Moës, and B. Burgardt. Improved implementation and robustness study of the X-FEM for stress analysis around cracks. *International Journal for Numerical Methods in Engineering*, 64(8):1033–1056, 2005.

[52] J. Rannou, A. Gravouil, and M. C. Baetto-Dubourg. A local multigrid X-FEM strategy for 3-D crack propagation. *International Journal for Numerical Methods in Engineering*, 77(4):581–600, 2008.